

## A model of tidally dominated ocean processes near ice shelf grounding lines

Paul R. Holland<sup>1</sup>

Received 4 October 2007; revised 30 June 2008; accepted 15 August 2008; published 1 November 2008.

[1] Glaciological processes at grounding lines, which divide floating ice shelves from grounded ice sheets, may strongly influence the dynamics and evolution of inland ice. Therefore, understanding the oceanic forcing on ice shelves in this region is of importance to predictions of cryospheric change and sea level rise. As the ocean cavity shallows toward the grounding line, tidal mixing becomes proportionately more important until a tidal front forms, beyond which the water properties are vertically homogenized. The extent of this mixed zone is relevant to several questions because a fully mixed region behaves differently to the stratified ocean offshore. In this study a highly simplified one-dimensional model is used to examine the size, properties, and sensitivities of the mixed zone. The model suggests that most grounding line mixed zones are small, implying that the usual models representing a stratified ocean are generally valid if tidal mixing is also taken into account. Modeled mixed zones can be significant in near-freezing regions with vigorous tides and a shallowly sloping cavity, but even these areas are smaller than previously proposed. It therefore seems that upwelling of warm water, rather than mixing in tidal zones, generally maintains ice shelf basal melting near grounding lines. Where mixed zones are present, the model suggests that they insulate the grounding line from offshore ocean waters. The model illustrates the origin of Ice Shelf Water plumes and confirms that unlike elsewhere in the cavity, melting in the mixed zone increases linearly in response to ocean warming.

**Citation:** Holland, P. R. (2008), A model of tidally dominated ocean processes near ice shelf grounding lines, *J. Geophys. Res.*, *113*, C11002, doi:10.1029/2007JC004576.

### 1. Introduction

[2] Ice shelves are the floating extension of grounded ice sheets, and a grounding line is the locus of points at which an ice shelf goes afloat. As ice shelves oscillate in response to tidal motion, grounding lines form a moving lateral boundary to the ocean cavity beneath. In reality, the grounding “line” is probably a collection of small-scale features upon which the ice shelf periodically grounds in analogy to the larger “ephemeral groundings” observed by *Schmeltz et al.* [2001]. Although grounding lines usually divide fairly sedentary floating and grounded parts of an ice sheet, they are of particular interest at the downstream limit of faster flowing ice streams, which commonly terminate in deep water at the landward end of ocean embayments.

[3] Understanding dynamic mass loss from ice sheets could significantly improve our ability to account for and predict sea level rise [*Intergovernmental Panel on Climate Change*, 2007]. In particular, observed thinning of ice streams in the Amundsen Sea embayment [*Wingham et al.*, 2006] has led to concern about the long-term stability of the West Antarctic Ice Sheet and its consequences for sea

level. The thinning has been accompanied by ice stream acceleration [*Joughin et al.*, 2003], grounding line retreat [*Rignot*, 1998] and downstream ice shelf thinning [*Shepherd et al.*, 2004], leading to a consensus that increased oceanic melting is the ultimate driver of the inland changes. The view that ice sheet behavior can be strongly responsive to the cryospheric processes coupling ice sheets to ice shelves at grounding lines is widely held [*Weertman*, 1974; *Schoof*, 2007]. There are many studies of the oceanic processes occurring beneath ice shelves, but none examining in detail the complex processes affecting basal melting in the vicinity of grounding lines.

[4] The largest ice shelves have horizontal dimensions of 100–500 km (e.g., Ross Ice Shelf (RIS), Filchner-Ronne Ice Shelf (FRIS)) and are melted slowly by cold and saline High-Salinity Shelf Water (HSSW) that is formed from brine rejected by sea ice growth offshore of the ice front and subsequently flows down seabed slopes toward deep grounding lines. The meltwater from these ice shelves influences the properties of Antarctic Bottom Water, which partly drives the global thermohaline circulation [*Orsi et al.*, 1999]. Some smaller (10–100 km) ice shelves (e.g., Pine Island Glacier, George VI Ice Shelf) are melted more rapidly by direct intrusions of warmer Circumpolar Deep Water (CDW) into the ice shelf cavity from the Antarctic Circumpolar Current; these ice shelves are concentrated in West Antarctica and some are subject to the most significant recent thinning. In

<sup>1</sup>British Antarctic Survey, Cambridge, UK.

both cases, the largest melt rates are usually found near grounding lines at the termini of ice streams [Jenkins and Doake, 1991; Joughin and Padman, 2003; Payne et al., 2007], deeper regions where the least modified source water masses may contact the ice shelf base.

[5] The ocean beneath ice shelves is generally stratified because ascending meltwater-rich currents overlies denser intrusions of HSSW or CDW. It is common for oceanic moorings beneath ice shelves to observe vertically well-mixed layers at the upper and/or lower boundaries of the water column [Foster, 1983; Nicholls et al., 1991, 2004], although these features are not universal [Nicholls et al., 2001; Craven et al., 2004]. The layers are maintained by turbulence generated by velocity shear at the boundaries that results from both the tidal oscillation of the water column and the flow of the buoyant and dense plumes, with the relative importance of processes varying between ice shelves.

[6] Many aspects of the circulation beneath ice shelves have been described successfully by models that represent this stratified scenario [e.g., Gerdes et al., 1999; Jenkins and Holland, 2002; Holland and Feltham, 2006], but such models do not include variations in vertical mixing due to tidal velocity shear. Beneath some ice shelves tidal velocities can be significantly larger than the buoyancy-driven circulation, particularly in shallower regions [Makinson and Nicholls, 1999]. The turbulence that ensues can homogenize the water column whenever it is sufficient to overcome the stratifying buoyancy flux due to melting.

[7] MacAyeal [1984] (hereinafter referred to as M84) argued that tidal mixing should become more vigorous as the grounding line is approached because tidal velocities generally increase in areas where the cavity shallows. Upper and lower mixed layers would thicken toward the grounding line and should logically meet at a point, called a tidal front, that forms the boundary between a vertically uniform region inshore and the stratified ocean offshore. In fact, as the cavity shallows the power required to homogenize the water column against a given buoyancy flux decreases and destratification becomes more likely even in the absence of accelerated tidal flow. Nicholls et al. [2004] observed stratified and well-mixed waters on either side of a tidal front in a water column thickness gradient beneath western Ronne Ice Front (some distance from any grounding line).

[8] The tidal front is a widely observed phenomenon in coastal oceanography [O'Donnell, 1993], where tidal shear at the seabed and surface wind mixing work against the stratifying surface heat and freshwater fluxes. According to simple theory, a particular tidal power distributes a given surface buoyancy flux completely through a certain depth of water in steady state [Simpson and Hunter, 1974; Fearnhead, 1975], hereinafter referred to as the "critical depth." Given a tidal velocity and buoyancy flux that are constant as the water column shallows toward the coast, the water column inshore of the critical depth will be well mixed. Therefore, tidal fronts should form beneath ice shelves wherever there is a sufficient increase in the tidal velocity, decrease in the water column thickness, or decrease in the melt rate. An additional subtlety affecting tidal fronts in the ice shelf case is that the surface buoyancy flux (melting) is governed by ocean properties rather than being forced externally.

[9] This study aims to use a simple model of the mixed zone shoreward of the tidal front to understand ocean behavior near ice shelf grounding lines. Applying the concept of tidal fronts to ice shelves is not new, but by modeling them some implications of the theory will be clarified. In particular, it is possible to assess how different ocean forcings alter the distance of the tidal front from the grounding line and processes within the mixed zone.

[10] This work is relevant to several questions. Many authors suggest that ice shelf melting affects the stability of inflowing ice streams, but the pattern of melting in the important grounding line region is unknown. It is unclear to what extent melting near grounding lines is controlled by tidally mixed zones rather than entrainment of heat into the upper layer of stratified regions [Hemer et al., 2006], or how the melt rate varies within mixed zones. It has been hypothesized that warm source waters intrude closer to grounding lines in cavities where the water column thickness decreases sharply [Schoof, 2007]; mixed zone extent is relevant to this question because horizontal heat transport through a tidally mixed region will differ from that in an overturning stratified system.

[11] Rising plumes of Ice Shelf Water [Jenkins and Bombosch, 1995; Holland and Feltham, 2006] must evolve from an initial meltwater impetus, which could originate in the tidally mixed zone. Subglacial meltwater may be released to the ocean in pulses [Gray et al., 2005; Fricker et al., 2007], but little is known about the conditions into which it will emerge. A final hypothesis stems from the idea that in stratified regions ice shelf melting grows nonlinearly in response to ocean warming [M84; Holland et al., 2008]. Increased melting freshens the mixed layer underlying the ice shelf, accelerating it and generating more turbulence. Oceanic heat transfer to ice shelves is determined by turbulence and thermal driving, which thus both increase with warming, so overall the increase in the melt rate is above linear. Since the mixed zone is governed by tides it should not accelerate and its melt rate may instead rise linearly in response to warming.

[12] In the remainder of this paper, the proposed conceptual and mathematical models are presented before illustrative results are shown and the model sensitivity to variation in ocean forcing and modeling assumptions is investigated. Conclusions are drawn with respect to the questions raised above.

## 2. Model of the Tidally Mixed Zone

### 2.1. Conceptual Model

[13] The proposed ocean structure is pictured in Figure 1, though this progression only holds if the water column thickness decreases monotonically toward the grounding line; in reality the cavity can be highly convoluted because of basal crevassing [Corr et al., 2001] or uneven bedrock topography [Heinart and Riedel, 2007]. Throughout most of the cavity the ocean is stratified by the buoyancy of meltwater relative to the deep influx of heat and salt (region I). As the cavity shallows, the power required to completely mix the meltwater vertically decreases. The turbulent energy available from tidal stirring may also increase, so overall a well-mixed region should appear (region II).

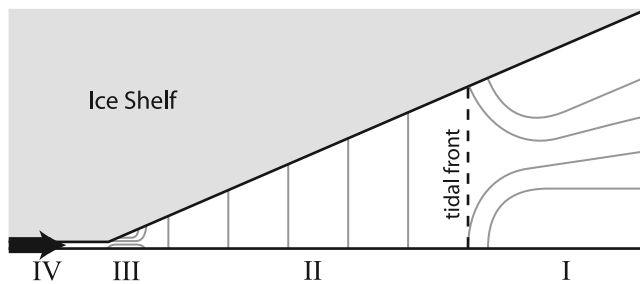


**Figure 1.** Schematic diagram of the conceptual model of the ocean near ice shelf grounding lines; gray lines are isopycnals. The majority of the ocean is stratified with mixed layers at the top and/or bottom of the water column (I), but a transition to vertically well-mixed conditions should occur as the grounding line is approached (II) because the water column shallows (less power is required to homogenize it vertically) and the tidal speed may increase. The water column may restratify very close to slowly moving grounding lines (III) because the tidal flow, and hence turbulent mixing, must then be small. A subglacial meltwater flux (IV) may promote or inhibit stratification near the grounding line depending upon its fluxes of turbulent kinetic energy and buoyancy. The bedrock is considered flat throughout this study, but sloping bedrock could be treated by a very similar model.

[14] If the grounding line moves slowly as the ice shelf flexes in response to the tide, the ocean could stratify close to the grounding line (region III) because the tidal excursion, and therefore the turbulence, decreases. Also, subglacial meltwater (region IV) will be of comparatively low salinity so if its flux is significant the water column properties will be determined by the kinetic energy and buoyancy flux of the meltwater inflow.

[15] The size of these different regions is governed by the subglacial meltwater flux and near-grounding-line profiles of tidal speed, water column thickness, and melt rate, none of which are well known because of the inaccessibility of ice shelf cavities. To make a first attempt at modeling the situation, it is therefore assumed that the subglacial meltwater flux is negligible, the cavity thickness increases linearly away from the grounding line, and the water column never restratifies as the grounding line is approached. These assumptions guarantee that a tidal front must occur, and the question then becomes the significance and properties of the mixed zone. The neglect of subglacial meltwater is probably quite widely applicable because there is some evidence that its flux is variable in time [Fricker *et al.*, 2007] and should be channeled into deep bedrock valleys, which are not the sole focus of this study.

## 2.2. Overview of the Mathematical Model

[16] Stringent assumptions are required to make the problem tractable, so it should be borne in mind that this study is intended to be a first modeling assessment of tidally mixed zones near grounding lines. The model represents only the region bounded by the grounding line and the tidal front, with the former fixed and the latter calculated as part of the solution procedure. The governing equations are averaged over the depth of the water column because

transported quantities are vertically uniform within the mixed zone by definition. The problem is reduced to one dimension in the cross-shore “longitudinal” direction by neglecting all variations parallel to the shore and thereby concentrating on processes responsible for positioning the tidal front. This orients the study toward embayed grounding lines, such as those where ice streams go afloat, rather than alternative cases in which alongshore transfer of heat and salt might be important. Longitudinal gradients arise because cold, fresh meltwater is released along the section while warmer, saline water is introduced only through the tidal front; the region is well mixed vertically but varies longitudinally because of the low aspect ratio of ice shelf cavities.

[17] This study strictly focuses on the most basic properties of the tidal front, so as a first approach all model quantities are averaged over a complete tidal cycle and a steady solution is sought. Amongst other things, this requires that the temporal motion of the tidal front is considerably smaller than its mean distance from the grounding line. This assumption depends upon the tidal ellipses, the vertical mixing time scale, and many other factors, and is impossible to test using the present model.

[18] Ocean flow within the mixed zone must also be idealized to make the problem tractable. Overturning flows driven by baroclinic instability necessarily cause vertical density variations, and therefore cannot be pervasive in a water column that has been determined to be vertically well mixed by tides. Extreme isolation also precludes direct mechanical forcing, so tidal flow should be of overwhelming importance overall. However, in order to proceed residual flows must be neglected so that the velocity averages to zero over a tidal cycle. Since the grounding line is sealed by neglecting subglacial meltwater, net longitudinal flow through the section, and advection across the tidal front, are ignored except where necessary to conserve mass.

[19] The treatment of the tidal velocity is therefore of paramount importance. As the tidal velocity vector rotates through a complete cycle, flow in the longitudinal plane of the section averages to zero. However, the instantaneous current is significant and vertical turbulent mixing, generated by shear, arises irrespective of the flow direction. Therefore, in this model the sole direct effect of tidal motion is to generate vertical turbulence. From this point of view, circular tidal ellipses generate turbulence equivalent to that of a steady current in any direction and degenerate or flat ellipses generate the same periodic turbulence as a fluctuating unidirectional flow. It is assumed here that the vertical turbulence generated by the rotating tidal current can be approximated by that of a steady flow at the mean tidal speed. As discussed later, this vertical turbulent mixing leads to horizontal dispersion when combined with a shear flow. Profiles of mean tidal speed and tidal dispersion, which is considered to be the primary horizontal transport mechanism, are fixed as external forcings on the model.

[20] The final model is illustrated in Figure 2 and described in more detail in the following sections. The water column thickness  $D$  is fixed according to the temporally averaged position of the ice shelf and increases linearly from the grounding line ( $x = 0$ ) to the tidal front ( $x = F$ ). Conserving meltwater mass, ordinary differential equations are formulated for the depth- and time-averaged heat and salt balances

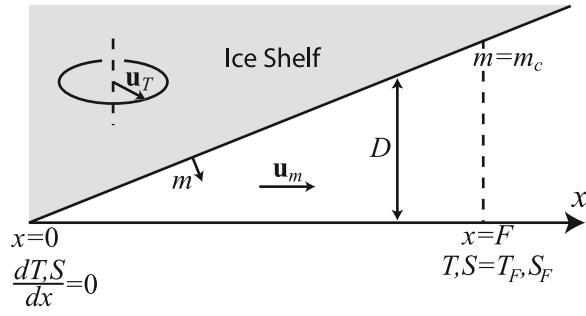


**Figure 2.** Schematic diagram of the model. The ocean cavity (thickness  $D$ ) is well mixed vertically but has properties that vary longitudinally from the grounding line ( $x = 0$ ) to the tidal front ( $x = F$ ). The varying melt rate  $m$  is maintained by horizontal tidal dispersion of heat and salt (caused indirectly by the rotating tidal vector  $\mathbf{u}_T$ ) from the tidal front toward the grounding line. Mass is conserved by a compensating meltwater flux  $\mathbf{u}_m$ . The tidal front is located where the melt rate equals the critical melt rate for stratification,  $m_c$ .

(section 2.3), subject to Dirichlet boundary conditions at the tidal front (section 2.4). The tidal front heat and salt source generates an ice shelf melting profile  $m$  (section 2.5), and the tidal front is located wherever the melt rate equals  $m_c$ , the critical rate required to stratify the water column (section 2.6). Profiles of tidal speed (section 2.7) and attendant horizontal tidal dispersion (section 2.8) are imposed externally. A numerical procedure (section 2.9) is applied to solve the model in a range of physical settings (section 2.10).

### 2.3. Governing Equations

[21] The assumption of a steady ice shelf profile requires a flow of meltwater directly away from the grounding line,  $\mathbf{u}_m$ , to conserve mass within the section. The instantaneous depth-averaged velocity  $\mathbf{u} = \mathbf{u}_T + \mathbf{u}_m$  is therefore the sum of the rotating tidal component,  $\mathbf{u}_T$ , and this small velocity. The time-averaged velocity in the section,  $\langle \mathbf{u} \rangle$ , is that of the meltwater component only,  $U_m = \langle \mathbf{u}_m \rangle$ , because the tidal velocity averages to zero over a tidal cycle. However, the time-averaged speed,  $\langle |\mathbf{u}| \rangle$ , is taken to be that of the tidal component only,  $U = \langle |\mathbf{u}_T| \rangle$ , because it is instantaneously much larger than the meltwater flow.  $U_m$ , calculated as part of the solution procedure, is used in advection terms while  $U$ , imposed externally, governs the production of turbulence.

[22] Under these assumptions, mass is conserved by

$$\frac{d(DU_m)}{dx} = m. \quad (1)$$

The equations governing conservation of heat and salt in the depth-averaged system are similar to those of meltwater plumes beneath ice shelves [Jenkins and Bombosch, 1995]. The balance is between meltwater advection, horizontal tidal dispersion, and melt-related sources:

$$\frac{d(DU_m T)}{dx} = \frac{d}{dx} \left( K_h D \frac{dT}{dx} \right) + m T_b - \gamma_T U (T - T_b), \quad (2)$$

$$\frac{d(DU_m S)}{dx} = \frac{d}{dx} \left( K_h D \frac{dS}{dx} \right), \quad (3)$$

where  $T$  and  $S$  are the depth- and time-averaged temperature and salinity respectively,  $K_h$  is a horizontal tidal dispersion coefficient (as opposed to a turbulent diffusivity),  $\gamma_T$  is an exchange coefficient representing turbulent heat transfer toward the ice shelf and  $T_b$  is the ice shelf-ocean interface temperature.

### 2.4. Boundary Conditions

[23] The single meltwater boundary condition is obvious because no ice shelf meltwater flow occurs at the grounding line

$$U_m = 0 \quad (x = 0). \quad (4)$$

Boundary conditions for temperature and salinity are not as straightforward owing to the lack of observations near grounding lines and the unconventional nature of the tidal front boundary.

[24] Temperature and salinity at the tidal front are fixed independently of each other to values representing the depth average of conditions immediately offshore, i.e., at the nearest stratified water column to the grounding line

$$T = T_F \quad (x = F), \quad (5)$$

$$S = S_F \quad (x = F). \quad (6)$$

This is tantamount to asserting that a large region of horizontally uniform (but possibly vertically varying) ocean encloses the mixed zone. An alternative approach could be to split the external water column into a lower source water layer and an upper meltwater layer and then force the model with the depth average. Upper meltwater properties could be derived from the lower source water using a simple theory of water mass transformation effected by melting [Gade, 1979; Greisman, 1979]. The better constrained properties of the source CDW or HSSW could then be used as external forcings rather than the depth average properties of the water column. This approach is not pursued because it requires additional assumptions to derive the layer thicknesses.

[25] Zero-flux Neumann conditions are appropriate at the grounding line if a bedrock-like boundary prevails. Alternatively, Dirichlet conditions could be used, appropriate to the presence of subglacial meltwater (low salinity and relatively high temperature), ice shelf interface water (according to the aforementioned theory), or anywhere in between. Neumann conditions are the default choice for this study on the basis that the model equations are then freed to determine the importance of ice shelf meltwater near the grounding line

$$\frac{dT}{dx} = 0 \quad (x = 0), \quad (7)$$

$$\frac{dS}{dx} = 0 \quad (x = 0). \quad (8)$$

The impact of this assumption is later investigated in sensitivity studies.

### 2.5. Ice Shelf Melt Rate

[26] The ice shelf melting formulation is standard apart from the use of water column thickness instead of mixed layer thickness. Balances of heat and salt flux at the ice shelf-ocean boundary are formulated and the system is closed by constraining the interface temperature  $T_b$  and salinity  $S_b$  using a linearized pressure freezing temperature [Jenkins and Bombosch, 1995]:

$$c_0\gamma_T U(T - T_b) = m\mathcal{L} + mc_I(T_b - T_I), \quad (9)$$

$$\gamma_S U(S - S_b) = mS_b, \quad (10)$$

$$T_b = aS_b + b + c(B - D), \quad (11)$$

where  $c_0 = 3974 \text{ J kg}^{-1} \text{ }^\circ\text{C}^{-1}$  and  $c_I = 2009 \text{ J kg}^{-1} \text{ }^\circ\text{C}^{-1}$  are specific heat capacities of water and ice;  $\mathcal{L} = 3.35 \times 10^5 \text{ J kg}^{-1}$  is the latent heat of ice fusion;  $T_I = -25^\circ\text{C}$  is an illustrative ice shelf core temperature;  $\gamma_T$  and  $\gamma_S$  are turbulent heat and salt transfer coefficients;  $a = -0.0573^\circ\text{C psu}^{-1}$ ,  $b = 0.0832^\circ\text{C}$ , and  $c = -7.61 \times 10^{-4} \text{ }^\circ\text{C m}^{-1}$ .  $B = 500 \text{ m}$  is an illustrative grounding line depth used throughout this study; it plays an important role in determining the thermal driving through its effect on the local freezing temperature. The third term in (9) approximates the relatively small effect of heat conduction within the ice shelf [Holland and Jenkins, 1999]; salt diffusion is neglected. Equations (9)–(11) are combined to solve for  $S_b$  and thus  $m$  and  $T_b$ . Dimensionless transfer coefficients are given by

$$\gamma_T = \frac{c_d^{1/2}}{2.12 \ln(c_d^{1/2} UD/\nu_0) + 12.5\text{Pr}^{2/3} - 9}, \quad (12)$$

$$\gamma_S = \frac{c_d^{1/2}}{2.12 \ln(c_d^{1/2} UD/\nu_0) + 12.5\text{Sc}^{2/3} - 9}, \quad (13)$$

where  $c_d = 0.0025$  is the ice shelf drag coefficient,  $\nu_0 = 1.95 \times 10^{-6} \text{ m}^2 \text{ s}^{-1}$  is the molecular viscosity, and  $\text{Pr} = 13.8$  and  $\text{Sc} = 2432$  are molecular Prandtl and Schmidt numbers [Jenkins and Bombosch, 1995].

### 2.6. Critical Melt Rate

[27] It is assumed that the location of the tidal front is entirely determined by the local vertical balance between the tidal energy dissipation rate and the rate at which gravitational potential energy is removed from the water column by the surface buoyancy flux; for simplicity external forcings such as ocean flow are neglected. The theory used here [Simpson and Hunter, 1974; Fearnhead, 1975] was adapted to ice shelf cavities by M84.

[28] The theory assumes that energy transfer to small-scale turbulence near the seabed follows a quadratic drag law. A small fraction of this,  $\alpha$ , is actually used to destratify

the water column. The available turbulent power from the seabed is therefore

$$P_T = \alpha\rho c_d \langle |\mathbf{u}_T|^3 \rangle, \quad (14)$$

where  $\rho = 1030 \text{ kg m}^{-3}$  is the seawater density. It is assumed that (14) is also applicable to the ice shelf base (implying that drag coefficients are the same), so the total turbulent power is twice equation (14).

[29] The proportion of turbulence expended in destratifying the water column,  $\alpha$ , is poorly constrained. M84 used  $\alpha = 1\%$  and a value of  $1.5\%$  has been adopted by the ice shelf community [Makinson and Nicholls, 1999; Hemer *et al.*, 2006], but lower values of  $\approx 0.5\%$  appear to have subsequently become more widely accepted [Simpson *et al.*, 1985; Hearn, 1985]. In this study  $\alpha$  is assigned an intermediate default value of  $0.75\%$ , and the impact of variation in  $\alpha$  is later investigated in a sensitivity study.

[30] Determining  $\langle |\mathbf{u}_T|^3 \rangle$  requires specification of the tidal speed's temporal variation, entailing a loss of generality. Investigation of modeled tidal velocities from several sub-ice shelf locations shows that  $\langle |\mathbf{u}_T|^3 \rangle$  may reasonably be replaced by  $\mu \langle |\mathbf{u}_T|^3 \rangle = \mu U^3$ , where  $1.5 \leq \mu \leq 3$ . Specifically, RIS cavity model velocities from Padman *et al.* [2003] were investigated at the positions of assimilated ice shelf heights listed therein, while high-resolution model velocities beneath Filchner-Ronne, Amery, and George VI ice shelves (L. Padman, personal communication, 2008) were investigated at many locations including the assimilated height positions listed by Padman *et al.* [2002]. A default value of  $\mu = 2$  is used in this study. Significant nonlinearity in  $U$  does not occur elsewhere in the standard model, so variation in the temporal pattern of tidal speed may be investigated by varying  $\mu$ . Since  $\mu$  and  $\alpha$  only appear multiplied together, this issue is examined as part of the aforementioned study of sensitivity to  $\alpha$ .

[31] We now consider the power required to mix a given surface meltwater flux vertically through the entire water column. For simplicity, density is assumed a linear function of salinity only and meltwater is considered fresh. Given a meltwater flux into a thin surface layer, the power required to maintain a destratified water column with a middepth center of gravity in steady state is

$$P_D = m\rho\beta SgD/2, \quad (15)$$

where  $\beta = 8 \times 10^{-4} \text{ psu}^{-1}$  is the haline contraction coefficient and  $g = 9.81 \text{ m s}^{-1}$  is the gravitational acceleration (M84).

[32] If we now assume that the tidal front occurs at the point where the turbulent power equals the destratification power, we obtain a critical melt rate

$$m_c = \frac{4\alpha c_d \mu U^3}{\beta g S D}. \quad (16)$$

It is noteworthy that this bulk energy argument is correct while neglecting the detailed physics of pycnocline formation. Studies show that injecting meltwater into the turbulent boundary layer beneath an ice shelf would generally create a mixed layer underlain by a pycnocline

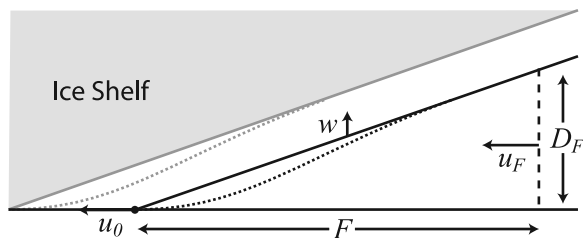


**Figure 3.** The principles underlying a longitudinally constant ocean flow speed. The ice shelf base is shown at high tide (gray lines) and low tide (black lines). The tidal speed beneath a realistic curved profile ice shelf (dotted lines) is approximated by that beneath a uniformly sloping ice shelf (solid lines). If the ice shelf oscillates vertically in a laterally uniform fashion, conservation of mass states that  $u_F D_F \approx wF$ , but  $F = D_F/D_x$  (denoting  $dD/dx$  by  $D_x$ ), so  $w \approx u_F D_x$ . Now, the grounding line motion is  $u_0 = w/D_x \approx u_F$ , so the instantaneous grounding line displacement approximately equals the offshore tidal excursion, and the tidal speed relative to the ice shelf may be assumed to be longitudinally constant.

that is eroded by turbulence from above and below; the supply of energy to the pycnocline depth determines its viability [Fearhead, 1975; Noh and Fernando, 1995]. A bulk argument is sufficient here because the energy flux through turbulent boundary layers is approximately uniform [Soulsby, 1983]. If mixing from above and below is equal, the steady pycnocline is always at the water column middepth [Makinson, 2002a, 2002b] and (16) is correct.

## 2.7. Profile of Tidal Speed

[33] The tidal forcing required by the model is the longitudinal profile of the tidal current speed averaged over a complete spring-neap cycle and the water column depth. This forcing is referred to as the “tidal speed” and governs turbulence in the melting parameterization (9)–(13), the critical melt rate (16), and (when used) the horizontal dispersion (17). In this section the longitudinal variation of this time- and depth-averaged speed (relative to its tidal front value) is analyzed by considering the equivalent variation in the instantaneous depth-averaged speed.

[34] To proceed, it is assumed that the tide moves the ice shelf up and down in a horizontally uniform manner and the ice shelf base has a uniform slope. As described in the caption to Figure 3, a simple geometrical argument then indicates that the grounding line moves back and forth at the instantaneous offshore ocean speed as the tide oscillates. If we now assume that the ice shelf moves in a purely vertical manner (its horizontal motion is small relative to ocean flow), the seawater instantaneously moves at the offshore speed relative to the ice shelf everywhere. This implies that after time averaging we may force the model with a spatially uniform tidal speed.

[35] There are many caveats to this argument. For example, the ice shelf elevation change may not balance the seawater volume flux, implying that a flood tide will be subject to vertical convergence toward the grounding line such that compensating horizontal divergence will cause acceleration. Alternatively, tidal energy is increasingly dissipated by drag and inelastic ice shelf flexure as the

grounding line is approached, so it is also possible that the tide decelerates as it heads inland. In this study the default forcing is a longitudinally constant speed profile, and other cases are tested by applying speed profiles determined by either a constant volume flux (acceleration) or a power law (deceleration) toward the grounding line.

## 2.8. Horizontal Tidal Dispersion Profile

[36] Fischer *et al.* [1979] list tidal dispersion coefficients of  $50\text{--}350\text{ m}^2\text{s}^{-1}$  derived from observation, varying between and within embayments. Geyer and Signell [1992] review a wide variety of tidal dispersion processes in bays and estuaries and cast doubt on the validity of using a tidal dispersion coefficient at all, but the crude approximation is probably appropriate to this simple model. Vigorously dispersive tidal processes are associated with the residual flows and complex topography neglected here. If the ocean oscillates uniformly within a cavity with no transverse geometry or current variations and no residual flow the dominant, though generally weak, mixing process is vertical shear dispersion (horizontal dispersion caused by vertical shear).

[37] Turbulent shear dispersion occurs when a filament of fluid distorted by shear is mixed by turbulence [Taylor, 1954]. In a pure oscillating flow, shear disappears when the flow is averaged over the period of oscillation, so the ratio between oscillation and turbulence time scales is critical [Okubo, 1967] (hereinafter referred to as O67). If the oscillation is much faster, shear distortion is irrelevant and dispersion is reduced; if mixing is complete within one oscillation, shear dispersion is analogous to that of steady flow [Holley *et al.*, 1970].

[38] The appropriate dispersion coefficient has been derived by O67 and others [Holley *et al.*, 1970; Fischer *et al.*, 1979]. The theory assumes a single oscillating harmonic constituent with linear vertical shear and no other variations, but it suffices for the present model. The O67 theory is adapted to the ice shelf cavity by applying the formula twice to half the water column thickness, assuming symmetry about the middepth, where the current amplitude is taken as  $2U$  to give the correct depth average. The final formula is

$$K_h = \frac{4U^2 \kappa P^2}{\pi^2 D^2} \left\{ 1 - \frac{4\kappa P}{D^2} \left[ \coth\left(\frac{D2}{2\kappa P}\right) - \operatorname{csch}\left(\frac{D2}{2\kappa P}\right) \right] \right\} \quad (17)$$

where  $\kappa = 5 \times 10^{-5}\text{ m}^2\text{s}^{-1}$  is used as an illustrative vertical turbulent eddy diffusivity [Gerdes *et al.*, 1999] and  $P = 23.93\text{ h}$  is the  $K_1$  tidal period dominant in the test case of section 3.1. A range of values could be used for the eddy diffusivity, and diurnal and semidiurnal tides vary in importance beneath different ice shelves [M84; Makinson and Nicholls, 1999; Hemer *et al.*, 2006].

[39] The default model application uses a uniform dispersion coefficient of  $K_h = 150\text{ m}^2\text{ s}^{-1}$  and variation in dispersive processes is then examined in a study of sensitivity to this value. Finally, the model most appropriate to the assumptions given here, equation (17), is considered.

## 2.9. Solution Procedure

[40] By reducing the problem to a heat balance only and making further assumptions, it would be possible to obtain a simple expression for the mixed zone length (investigated

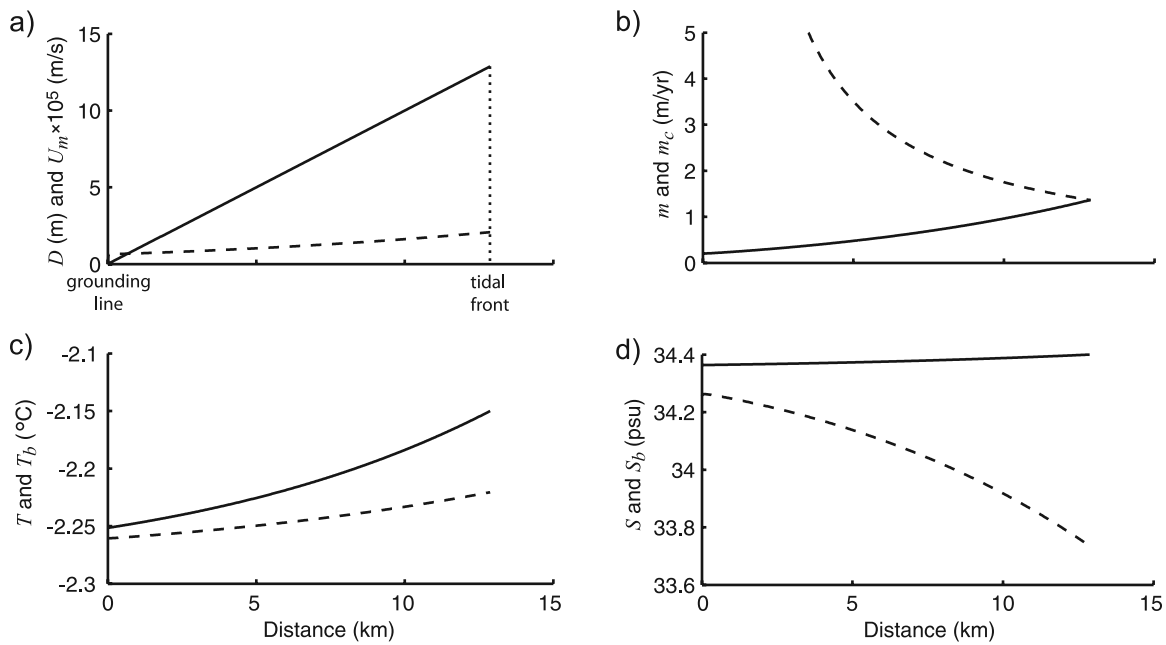


**Figure 4.** Results from the eastern RIS application of the model ( $T_F = -2.15^\circ\text{C}$ ,  $S_F = 34.4$  psu,  $D_x = 0.1\%$ , and  $U = 10$  cm  $\text{s}^{-1}$ ). (a) Water column thickness (solid line) and meltwater flow speed (dashed line), (b) melt rate (solid) and critical melt rate (dashed), (c) temperature (solid) and interface temperature (dashed), and (d) salinity (solid) and interface salinity (dashed).

later; see section 3.2) and a heat equation that is solvable analytically. However, the results are of limited applicability. Therefore, a numerical procedure is used to determine the tidal front location and ocean property profiles within the mixed zone. This enables the additional complexities described above to be incorporated into the model, including a full melt rate formulation, salt and meltwater balances, and longitudinal variation in tidal forcing.

[41] A large initial guess of the tidal front position initiates the iterative solution procedure. On each iteration heat, salt, and meltwater equations are solved (with  $T_F$  and  $S_F$  boundary conditions applied at the current tidal front) and the resulting melt rate profile is compared to the critical profile to determine which part of the domain, if any, should in fact be stratified. The tidal front is retracted to the new location and the process is repeated until the tidal front position converges.

[42] The model is implemented in the Matlab problem solving environment and during each iteration the system of ordinary differential equations is solved using a sixth-order-accurate extension [Hale, 2006] to the boundary value problem solver of Kierzenka and Shampine [2001]. This solver uses a collocation method (akin to Simpson's method), approximating the solution by a piecewise-quintic polynomial whose coefficients are determined by solving iteratively a system of nonlinear algebraic equations. The method adapts the mesh and estimates error according to the local residual of the polynomial.

## 2.10. Physical Forcing Parameters

[43] The model requires four external forcings: temperature and salinity at the tidal front ( $T_F$ ,  $S_F$ ), the cavity thickness, set according to its slope ( $D_x = dD/dx$ ), and the

offshore tidal speed ( $U$ ). In this section the range of forcings used in each of the sensitivity studies is defined.

[44] Seawater temperature is relatively well constrained by source water masses; HSSW cannot be cooler than  $-1.9^\circ\text{C}$  (the surface freezing temperature) and CDW entering ice shelf cavities is generally little warmer than  $+1.0^\circ\text{C}$  [Jacobs *et al.*, 1996]. The “standard case” Pine Island Glacier model results of Hellmer *et al.* [1998] suggest that unmodified CDW may penetrate the cavity to the grounding line. Larger ice shelves will cool source waters significantly by diluting them with meltwater; temperatures of  $-2.5^\circ\text{C}$  have been recorded beneath FRIS [Nicholls *et al.*, 2001]. The minimum forcing temperature must exceed the local freezing temperature, so the range tested here is  $-2.2$  to  $+1.5^\circ\text{C}$ .

[45] Salinities between 34.2 and 34.85 psu have been observed beneath and offshore of ice shelves [Jacobs *et al.*, 1979, 1996; Nicholls *et al.*, 2004; Makinson *et al.*, 2006], so the upper bound is 34.9 psu. The lower bound should also consider the maximum conceivable meltwater freshening. If CDW is cooled and freshened to a deep water freezing temperature, salinities as low as 33.6 psu are theoretically possible [Jenkins, 1999]; though unlikely, this value is taken as the lower bound.

[46] Relevant seabed topography is difficult to measure because radar cannot penetrate seawater and seismic data are difficult to interpret near grounding lines [Johnson and Smith, 1997]. Nevertheless, seismic records can determine average water column thickness slopes near grounding lines and minima and maxima for each ice shelf may be summarized as follows: 0.05% in eastern RIS cavity but 1.5% to the west [Greischar and Bentley, 1980]; 0.5% south of Henry Ice Rise and 10% west of Korff Ice Rise [Johnson

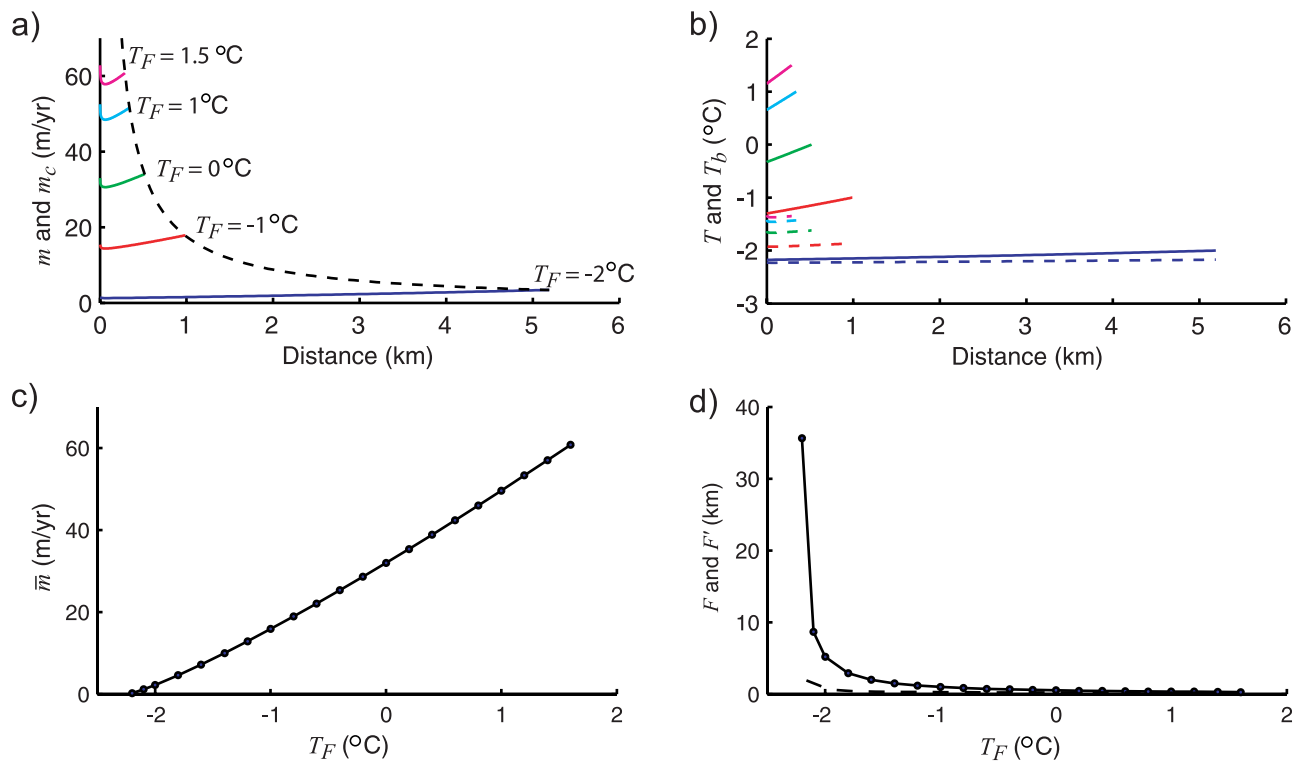


**Figure 5.** Sensitivity of model results to variation in tidal front temperature ( $T_F$  varied between  $-2.2^\circ\text{C}$  and  $+1.5^\circ\text{C}$  while  $S_F = 34.4$  psu,  $D_x = 0.1\%$ ,  $U = 10$   $\text{cm s}^{-1}$ ). (a) profiles of melt rates (solid) and critical melt rate (dashed) for different cases, (b) profiles of temperature (solid) and interface temperature (dashed), (c) variation of section average melt rate with tidal front temperature, (d) variation of tidal front position with tidal front temperature predicted by the model (solid) and a simple analytical relation (dashed).

and Smith, 1997] and 0.05% along Rutford Ice Stream inlet but over 5% across it [Smith and Doake, 1994], all beneath FRIS; 2% and 8% beneath southern George VI Ice Shelf [Maslanyj, 1987]; 1.5% near Jutulgryta and 10% elsewhere beneath Fimbul Ice Shelf [Nøst, 2004]; 0.5% and 1.5% beneath central Amery Ice Shelf [Hemer et al., 2006]. The thickness slope is therefore varied between 0.05% and 10%.

[47] Sub-ice shelf tidal current observations of the length required to assess average speeds are extremely rare. Beneath FRIS, mean tidal speeds are  $\approx 16\text{--}35$   $\text{cm s}^{-1}$  in Ronne Depression [Nicholls et al., 2004],  $\approx 20$   $\text{cm s}^{-1}$  further south [Nicholls, 1996], and  $\approx 5$   $\text{cm s}^{-1}$  near Korff Ice Rise [Nicholls et al., 1997]. Observations limit George VI Ice Shelf mean tidal speeds to  $\approx 5$   $\text{cm s}^{-1}$  near the northern ice front [Loynes et al., 1984; Potter and Paren, 1985] and lower near the southern end [Potter et al., 1985]. Modeling efforts are more common; Makinson and Nicholls [1999] found mean FRIS model tidal speeds of up to 50  $\text{cm s}^{-1}$  near the ice front and 30  $\text{cm s}^{-1}$  south of Henry Ice Rise, but generally lower elsewhere at a few centimeters per second; Padman et al. [2003] found mean tidal speeds of less than 10  $\text{cm s}^{-1}$  beneath the majority of RIS; Hemer et al. [2006] found peak tidal speeds less than 10  $\text{cm s}^{-1}$  under most of Amery Ice Shelf. The mean tidal speed is varied between 1  $\text{cm s}^{-1}$  and 15  $\text{cm s}^{-1}$  in this study. For comparison, models predict that rising meltwater plumes associated with the buoyancy-driven circulation

attain speeds of up to 1  $\text{cm s}^{-1}$  beneath RIS [Holland et al., 2003] and 50  $\text{cm s}^{-1}$  beneath Pine Island Glacier [Payne et al., 2007]; the relative importance of buoyancy and tides clearly varies considerably.

### 3. Results

[48] In this section the model is applied to an illustrative scenario and then employed in studies of sensitivity of the results of this case to variation in physical forcings and modeling choices.

#### 3.1. Ross Ice Shelf

[49] To illustrate the general properties of the mixed zone, the model is applied to the ocean cavity beneath the eastern side of RIS, south of Roosevelt Island. Here the mixed region is unusually large (M84 proposes a mixed zone extent of 100 km) because the water column thickness slope is extremely small ( $D_x = 0.1\%$  [Greischar and Bentley, 1980; Albert and Bentley, 1990]) and tidal velocities are relatively high ( $U = 10$   $\text{cm s}^{-1}$  [Padman et al., 2003], though M84's tidal energy dissipation rates are consistent with slightly higher tidal speeds). There are few nearby measurements of  $T_F$  and  $S_F$  and ocean models have not accurately resolved the topography of such a shallow cavity [Assmann et al., 2003; Holland et al., 2003; Dinniman et al., 2007], so  $T_F = -2.15^\circ\text{C}$  and  $S_F = 34.4$  psu are used, representative of the meltwater layer beneath the J9 borehole site further south [Foster, 1983].

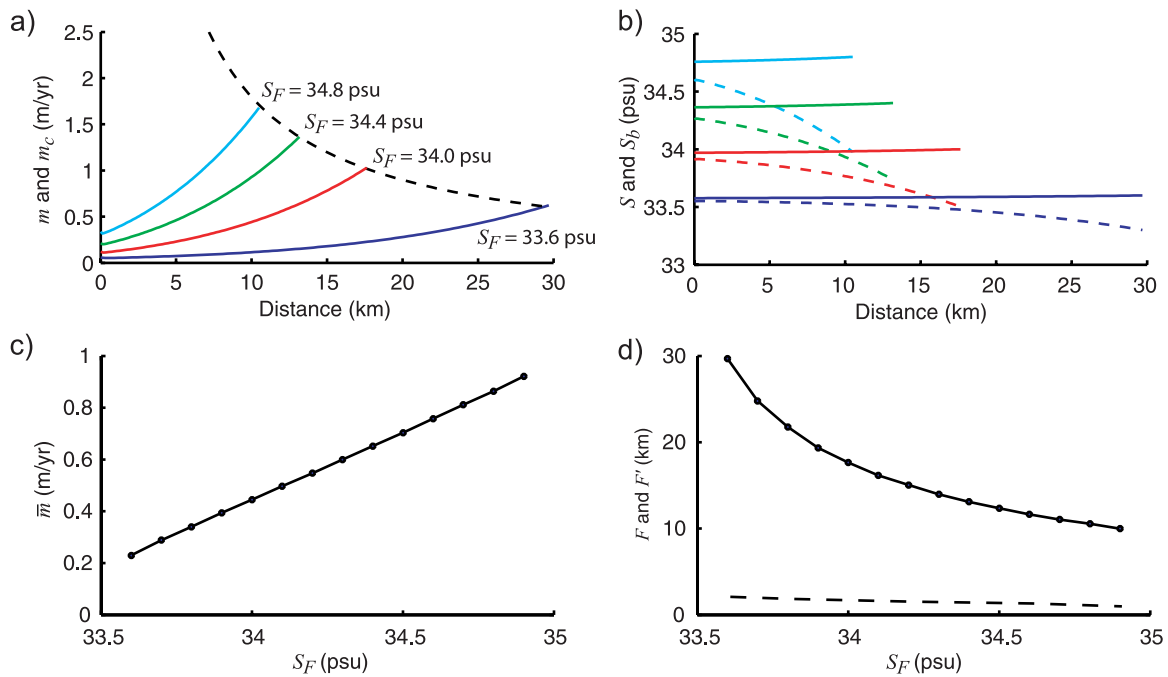


**Figure 6.** Sensitivity of model results to variation in tidal front salinity ( $S_F$  varied between 33.6 psu and 34.9 psu while  $T_F = -2.15^\circ\text{C}$ ,  $D_x = 0.1\%$ , and  $U = 10 \text{ cm s}^{-1}$ ). (a) Profiles of melt rates (solid) and critical melt rate (dashed) for different cases, (b) profiles of salinity (solid) and interface salinity (dashed), (c) variation of section average melt rate with tidal front salinity, and (d) variation of tidal front position with tidal front salinity predicted by the model (solid) and a simple analytical relation (dashed).

[50] The model predicts a tidal front 12.9 km from the grounding line where the water column thickness is 12.9 m (Figure 4a). The critical melt rate increases sharply toward the grounding line in inverse proportionality to water column thickness (Figure 4b and equation (16)), while the melt rate decreases shoreward of the tidal front (Figure 4b) because meltwater release cools the ocean (Figure 4c). The salinity does not vary significantly, but the interface salinity decreases as the melt rate grows toward the tidal front (Figure 4d), which raises the interface temperature slightly (Figure 4c). The meltwater flux is small (Figure 4a).

[51] Despite favorable forcings, the model predicts a mixed zone an order of magnitude smaller than suggested by M84. In that study, tidal zone lengths are determined by the logic that melt rates should not exceed  $0.05\text{--}0.5 \text{ m a}^{-1}$ , so that any area with a critical rate above this must be well mixed. Here the procedure is to choose tidal front temperature and salinity conditions, convert the resulting melt rate into a critical depth by equating it to the critical melt rate, and convert this into a horizontal length using the water column thickness slope. A tidal front thermal driving ( $T - T_b$ ) of  $0.07^\circ\text{C}$  melts  $1.5 \text{ m a}^{-1}$  of ice in a current of  $U = 10 \text{ cm s}^{-1}$  (Figure 4b), so it is obviously the higher melt rate here that produces the smaller mixed zone; a fuller comparison of the two models is presented in section 4. The melt rate is probably too large for the region, suggesting an excessively high thermal driving or flow speed, so the model sensitivity to variation in ocean forcings is now

tested by varying each of  $T_F$ ,  $S_F$ ,  $D_x$  and  $U$  in turn while keeping the others fixed at the RIS values.

### 3.2. Sensitivity to Ocean Forcings

[52] Varying each of  $T_F$  and  $S_F$  alters the location of the tidal front and the properties of the mixed zone but leaves the critical melt rate unaffected (Figures 5a and 6a). As  $T_F$  or  $S_F$  is increased the tidal front melt rate rises, reducing the water column thickness that can be destratified by the given turbulence and thus retracting the tidal front to a shallower location (Figures 5a and 6a). Temperatures or salinities throughout the mixed region are increased relative to interface values (Figures 5b and 6b), raising section-averaged melt rates (Figures 5c and 6c).

[53] The melt rate changes linearly in response to temperature variations, with a higher sensitivity ( $\approx 17 \text{ m a}^{-1} \text{ }^\circ\text{C}^{-1}$ ) than found by *Rignot and Jacobs* [2002] and *Shepherd et al.* [2004]. However, the mixed region is generally small (Figure 5d), with  $F < 10 \text{ km}$  for  $T_F > -2^\circ\text{C}$  and  $F < 1 \text{ km}$  for  $T_F > -1^\circ\text{C}$  (relative to a grounding line freezing point of  $-2.27^\circ\text{C}$ ), limiting the applicability of this linear sensitivity. The melt rate rises linearly with salinity, but the response is much weaker.

[54] These linear increases in melt rate produce above-linear decreases in mixed zone size because the critical melt rate is inversely proportional to  $D$  (Figure 5). At colder temperatures, melt rates equal  $m_c$  in a region of the curve that varies slowly with  $D$  (Figure 5a), so  $F$  depends strongly upon  $T_F$  because small melt rate changes require large depth changes to restore the  $m = m_c$  balance. Conversely,  $F$  is

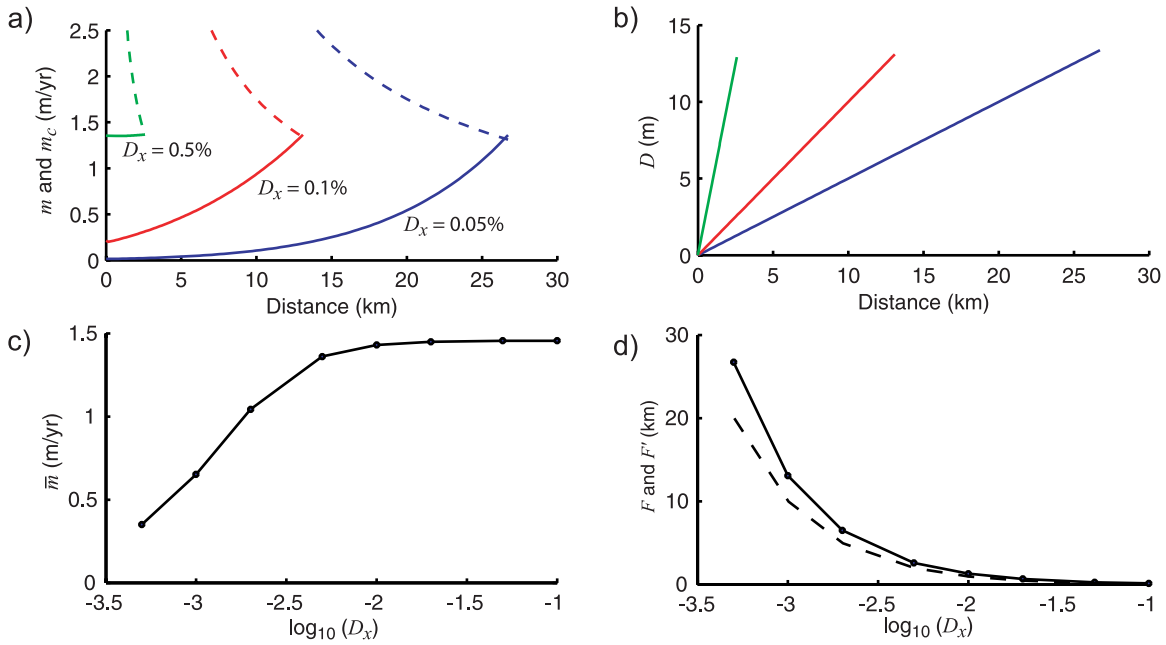


**Figure 7.** Sensitivity of model results to variation in water column thickness slope ( $D_x$  varied between 0.05% and 10% while  $T_F = -2.15^\circ\text{C}$ ,  $S_F = 34.4$  psu, and  $U = 10$  cm  $\text{s}^{-1}$ ). (a) Profiles of melt rates (solid) and critical melt rate (dashed) for different cases, (b) profiles of water column thickness, (c) variation of section average melt rate with slope, and (d) variation of tidal front position with slope predicted by the model (solid) and a simple analytical relation (dashed).

insensitive to variations in  $T_F$  applicable to warmer-water ice shelves. Salinity variation encompasses a smaller range of sensitivities (Figures 6a and 6d).

[55] Varying water column thickness slope has a strong influence on tidal front position because it directly alters the distance of the given critical depth from the grounding line (Figures 7a and 7b). As the tidal front retreats with increasing slope, the larger melt rates near the tidal front occupy a greater proportion of the section, so the mean rate converges to the tidal front value (Figure 7c).

[56] The effect of varying  $U$  is more complex because its choice affects both the melt rate and the critical rate. Raising  $U$  increases  $m_c$  (Figure 8a), enlarging the mixed zone produced by a given melt rate. However, it also increases the melt rate, introducing a (smaller) counterbalancing effect (Figure 8d). A maximum occurs in the average melt rate (Figure 8c) because decreasing  $U$  from this value reduces the tidal front melt rate and increasing  $U$  contracts the proportion of the domain over which this melt rate dominates.

[57] Variations in  $F$  may be investigated by introducing a simple relation that predicts  $F'$ , the approximate tidal front position, as plotted on Figures 5d, 6d, 7d, and 8d. Since the tidal front occurs when melting equals the critical rate, we reconsider the melt rate formulation (9)–(13) to derive  $F'$ . The system can be simplified by fixing  $\gamma_T$  and  $T_b$  to constant values,  $\gamma'_T$  and  $T'_b$ , which amounts to ignoring the effect of salinity on melting; the validity of this approach is examined by Holland and Jenkins [1999]. The melting formulation is then contained in equation (9), and additionally neglecting heat conduction leads to

$$m' = \frac{c_0 \gamma'_T U (T - T'_b)}{\mathcal{L}}. \quad (18)$$

The denominator in  $\gamma_T$  (equation (12)) varies slowly, and testing shows that  $\gamma_T \approx 6 \times 10^{-4}$  over the parameter range of interest here. The effect of salinity may be approximated by dividing  $\gamma_T$  by 1.6 [Holland and Jenkins, 1999], so  $\gamma'_T = 4 \times 10^{-4}$ .  $T'_b$  is the freezing temperature (11) at the grounding line depth and tidal front salinity. Equating (18) to the critical rate (16), evaluating all properties at the tidal front, and setting  $F' = D_F D_x$ , we obtain

$$F' = \frac{4\alpha c_d \mathcal{L} \mu U_F^2}{\beta g c_0 \gamma'_T S_F (T_F - T'_b) D_x}, \quad (19)$$

an expression for the tidal front location in terms of the forcing parameters.

[58]  $F'$  is notable in its failure in predicting  $F$  in Figures 5d and 6d and its relative success in Figures 7d and 8d. In cold-water cases (such as the default case here) temperatures are close to the in situ freezing point, which increases with distance from the grounding line and thereby reduces the melt rate.  $F'$  cannot represent this effect because it neglects depth variations, so it underpredicts  $F$  in Figures 5d and 6d.  $F'$  cannot qualitatively represent the variation in  $F$  with  $S_F$  either (Figure 6d) because salinity is constant in its derivation. Both findings demonstrate that using the full melting formulation and a salt balance is important under the assumptions of this study. In contrast,  $F'$  is a good predictor of the inverse proportionality of  $F$  to variation in  $D_x$  (Figure 7d).  $F'$  is proportional to  $U^2$  as a result of assuming that  $m \propto U$  and  $m_c \propto U^3$ , and this appears to be a fair, though imperfect approximation (Figure 8d);  $F'$  incorporates a higher melt rate because of its neglect of freshening and therefore underpredicts  $F$ .

[59] The model cannot permit  $T_F$  values below  $-2.2^\circ\text{C}$  or  $U$  above  $15$  cm  $\text{s}^{-1}$  in these tests. For each  $T_F$  and  $S_F$ , tidal

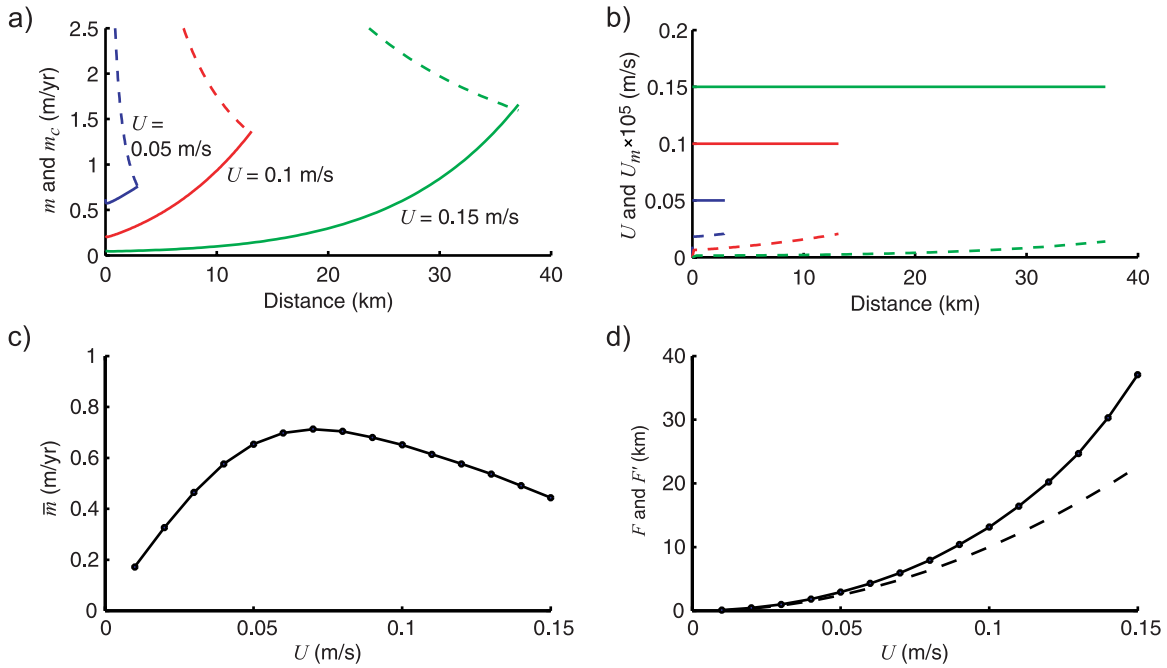


**Figure 8.** Sensitivity of model results to variation in tidal speed ( $U$  varied between  $1 \text{ cm s}^{-1}$  and  $15 \text{ cm s}^{-1}$  while  $T_F = -2.15^\circ\text{C}$ ,  $S_F = 34.4 \text{ psu}$ , and  $D_x = 0.1\%$ ). (a) Profiles of melt rates (solid) and critical melt rate (dashed) for different cases, (b) profiles of tidal speed (solid) and meltwater flow speed (dashed), (c) variation of section average melt rate with tidal speed, and (d) variation of tidal front position with tidal speed predicted by the model (solid) and a simple analytical relation (dashed).

front melting decreases slowly in  $x$  because  $T_b$  increases as the ice shelf base shallows. The resultant tidal front melting curve must intersect the critical melting curve to locate the tidal front. The critical rate sometimes decreases so slowly

in  $x$  that an intersection never occurs, so forcings that produce a large mixed zone may not possess a solution. This is ultimately a weakness of the model setup, because in reality the “external” temperature would not be spatially

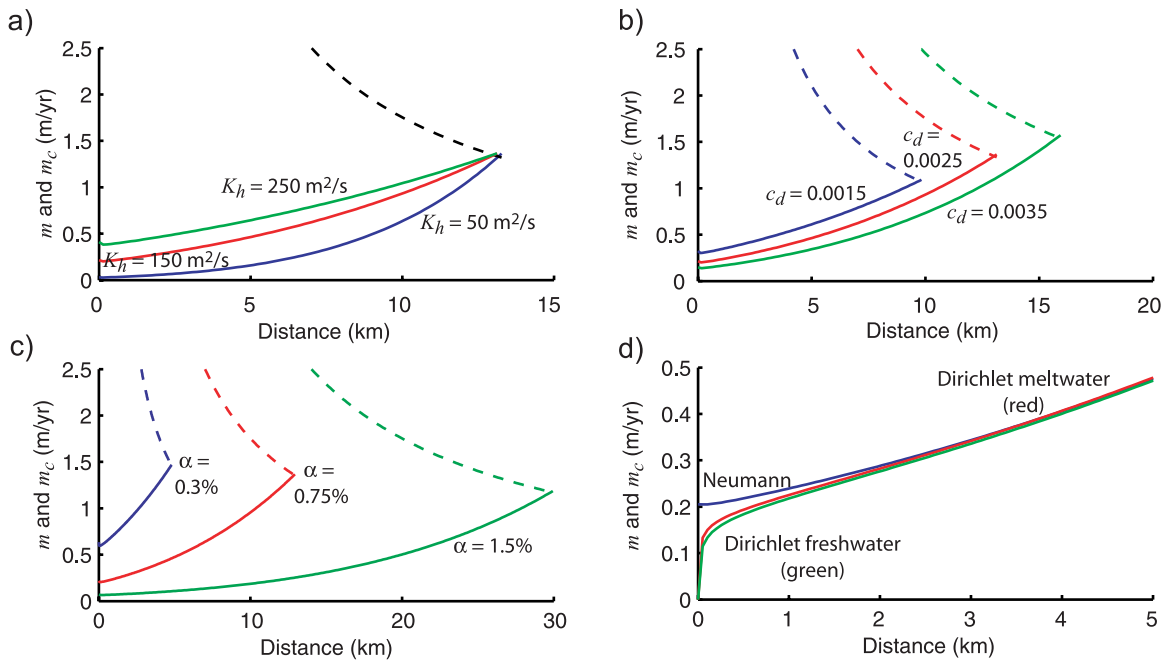


**Figure 9.** Sensitivity of melt rate profiles to variation in modeling choices ( $T_F = -2.15^\circ\text{C}$ ,  $S_F = 34.4 \text{ psu}$ ,  $D_x = 0.1\%$ , and  $U = 10 \text{ cm s}^{-1}$ ). (a) Horizontal dispersion coefficient varied, (b) drag coefficient varied, (c) proportion of turbulence used in destratification varied, and (d) grounding line boundary condition varied. Note the different scales used in each plot.

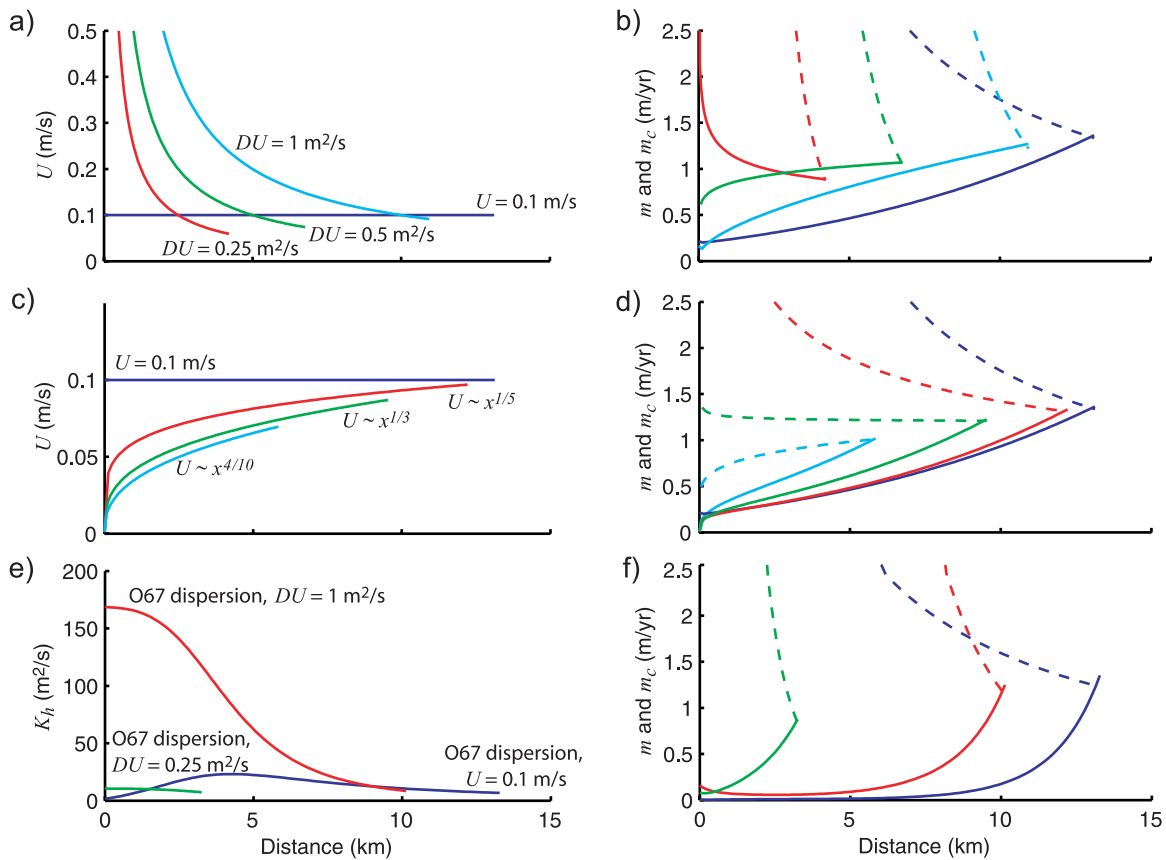


**Figure 10.** Sensitivity of model results to variation in profiles of tidal speed and dispersion coefficient ( $T_F = -2.15^\circ\text{C}$ ,  $S_F = 34.4$  psu,  $D_x = 0.1\%$ , and  $U = 10$  cm s $^{-1}$ ). (a and b) Speed and melt rate for cases with spatially constant volume flux, (c and d) speed and melt rate for power law boundary layer cases, and (e and f) dispersion coefficient and melt rate for O67 dispersion coefficient cases.

uniform.  $U = 15$  cm s $^{-1}$  is a reasonable upper bound everywhere apart from south of Henry Ice Rise, FRIS, which experiences tidal speeds of 30 cm s $^{-1}$  and may therefore support a large mixed zone. The model does not fail for this region because steeper bedrock slopes alleviate the problem described above, but the solution is not pursued here in favor of investigating general tidal front properties.

### 3.3. Sensitivity to Modeling Choices

[60] In this section the sensitivity of results to variation in model assumptions and parameters is tested, again by varying quantities individually from their default values. Varying the tidal dispersion coefficient  $K_h$  alters the transport of heat and salt from the tidal front toward the grounding line, affecting the melt rate profile, but does not change the tidal front location (Figure 9a). Increasing the drag coefficient  $c_d$  raises the critical rate and (to a lesser extent) the melt rate (Figure 9b), enlarging the mixed zone overall.

[61] Considerable uncertainty exists in the best choice of  $\alpha$ , and values in the range 0.3–1.5% have been quoted in the relevant literature (see section 2.6).  $F'$  suggests that the tidal front location is linearly related to  $\alpha$  through its effect upon the critical melt rate, and Figure 9c shows that the full model supports this prediction. The uncertainty in  $F'$  that arises from  $\alpha$  is a significant model weakness and, importantly, will also be present in all other studies using the critical melt rate (16).

[62] As discussed in section 2.6, varying  $\alpha$  in this model may also be taken to crudely represent different temporal variability in the tidal speed; higher values represent more variable tidal forcings because variation increases  $\langle |\mathbf{u}_T|^3 \rangle$  relative to  $\langle |\mathbf{u}_T| \rangle^3$ . The 50% change in  $\mu$ , and hence  $\alpha$ , that can arise from this effect therefore introduces a similar additional uncertainty into the tidal front position.

[63] Figure 9d shows that the effect on melting of switching to Dirichlet conditions at the grounding line (see section 2.4) is confined to a very narrow region. This implies that little unusual melting or freezing is induced by subglacial meltwater in the rather special case that it sets grounding line ocean properties without affecting turbulence or requiring advection terms. The tidal front is unaffected because it is determined solely by offshore conditions. The melting profile of the subglacial meltwater case (freshwater at the local freezing point;  $T = -0.30^\circ\text{C}$ ,  $S = 0$  psu) is very similar to that of the ice shelf meltwater case (tidal front water reduced to the freezing point according to *Gade* [1979];  $T = -2.27^\circ\text{C}$ ,  $S = 34.36$  psu). Temperature and salinity profiles differ significantly between these cases but melt rates are virtually identical because both have freezing at the grounding line, standard thermal driving at the tidal front, and equal dispersion of heat and salt.

[64] Figures 10a and 10c show the different velocity profiles discussed in section 2.7. If the volume flux is assumed constant, the tidal speed increases sharply toward

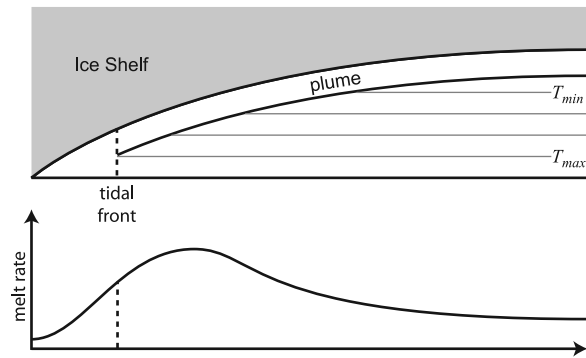


**Figure 11.** Generalization of the time-averaged ice shelf melt rate with distance from the grounding line. Melting increases toward the tidal front, where a plume is initiated. The melt rate generally continues to rise as the plume accelerates, mixing more heat toward the ice shelf, and then decreases as the freezing temperature increases, the ice shelf base flattens, and more modified (cooler) waters are encountered. This mean circulation is superimposed upon the tidal cycle, which can also be important for mixing heat into the plume. The size of the tidal zone is greatly exaggerated, and other plume behavior is possible.

the grounding line until values become unrealistic. This steepens the critical rate and eventually reverses the trend in the melt rate (Figures 10a and 10b). Decreasing the volume flux shortens the mixed zone because the critical rate steepens more toward the grounding line than the melt rate. Adopting power law velocity profiles that decelerate toward the grounding line from  $10 \text{ cm s}^{-1}$  at  $x = 15 \text{ km}$  (Figure 10c) also affects the critical rate more than the melt rate, reducing the mixed zone (Figure 10d). The  $m_c$  curve shallows as the velocity power law exponent is decreased, until it is almost flat when  $U \propto x^{1/3}$  because  $m_c \propto U^3$  in equation (16).

[65] Figures 10e and 10f show the effect of replacing the constant dispersion coefficient with the O67 tidal dispersion formulation. The default constant speed case produces a very weak dispersion using this formula, demonstrating the subtlety of vertical shear dispersion compared with other mechanisms. Similarly to uniform  $K_h$  reductions, the tidal front is unaffected but transport toward the grounding line is reduced. Experimentation with different vertical diffusivities and tidal periods shows that the O67 formulation can only give dispersion rates approaching those listed by Fischer *et al.* [1979] when combined with the assumption of a (high) constant volume flux, as used by Ou *et al.* [2003], but these velocities become excessive as the grounding line is approached. Therefore, using a constant dispersion coefficient to crudely represent unspecified mixing processes appears to be more reasonable than assuming that vertical shear dispersion is dominant.

#### 4. Discussion

[66] While bounded by observation, the default RIS forcings are chosen to produce a large mixed zone. However, the predicted mixed zone is still an order of magnitude smaller than that proposed by M84, an inconsistency so far

attributed to the high tidal front melt rate. Reducing  $T_F$  from its J9 meltwater value could be reasonable because J9 is shallower than the study region and its meltwater will thus be warmer than local meltwater. The  $T_F = -2.2^\circ\text{C}$  case (the coldest possible; see section 3.2) has a tidal front melt rate of  $0.5 \text{ m a}^{-1}$ , which seems reasonable given that it moderately exceeds the cavity average of  $0.22 \text{ m a}^{-1}$  [Jacobs *et al.*, 1992] and the results of numerical models [Assmann *et al.*, 2003; Holland *et al.*, 2003; Dinniman *et al.*, 2007], which do not incorporate the active tides in this region. However, at 35 km in length the mixed zone is still significantly shorter than M84 proposes. If it were possible, reducing the temperature further might enlarge the mixed zone, but that would imply a thermal driving of less than  $0.07^\circ\text{C}$  (and tidal currents of  $10 \text{ cm s}^{-1}$ ) over this large area.

[67] Sensitivity to modeling parameters can account for the remainder of the discrepancy because M84 used a higher  $\alpha$  and the appropriate value of  $\mu$  could be larger than 2. If  $F$  is linearly related to  $\alpha\mu$  then setting  $\alpha = 1\%$  and  $\mu = 3$  would double the mixed zone length to 70 km in the  $T_F = -2.2^\circ\text{C}$  case mentioned above. M84 states that his mixed zone sizes are probably upper bounds and estimates their uncertainty to be 50 km, so overall the discrepancy appears to be resolvable by choosing different values of  $T_F$ ,  $\alpha$ , and  $\mu$  to the standard values justified in this study.

[68] The discussion so far applies only to the special conditions required to produce significant mixed zones, whose exact extent cannot be predicted in any case because of the assumptions of the model and the demonstrated sensitivity to modeling parameters. A more robust finding is that for the majority of reasonable forcings the tidal zone is so small and insensitive to forcing variation that its effects can generally be neglected. Tidal zones should exist next to most grounded ice, but significant tidal zones only exist in shallowly sloping cavities with large tidal velocities and temperatures marginally above freezing. This suggests that ice shelf melting near grounding lines is overwhelmingly supported by entrainment of heat into upper mixed layers, as found by Hemer *et al.* [2006], rather than the mixing in tidal zones suggested by M84. This does not imply that tides are negligible, because tidal dissipation is implicated in the entrainment process. Also, this does not apply to mixed zones that cannot be characterized as being next to grounding lines according to the assumptions of this model (e.g., over Berkner Bank, Ronne Ice Front [Makinson and Nicholls, 1999]).

[69] Tidal fronts are the “birthplace” of Ice Shelf Water plumes because they are the shoreward stratification limit and therefore the first point at which a plume can exist. Where subglacial meltwater is negligible, the fixed property regions used to initiate Ice Shelf Water plume models [Jenkins and Bombosch, 1995; Holland and Feltham, 2006] should represent conditions immediately offshore of a tidal front. Tidal fronts tend to oscillate (relative to the grounding line in the present case) as the tidal power varies, particularly during the spring-neap cycle [Simpson and Bowers, 1981], and this could periodically restratify pulses of water from which the upper layer subsequently develops into plumes.

[70] Uniquely, the model predicts properties within the mixed zone, suggesting that melting decreases inshore of the tidal front because meltwater cooling is not countered by

any heat source. This contributes to a general picture of mean melt rate evolution along an ice shelf (Figure 11). Melting is weaker near the grounding line, where the water column is well mixed and meltwater is influential. It grows as distance from the grounding line increases until a pycnocline appears, at the tidal front, beyond which a meltwater-rich upper layer overlies warmer water. The melt rate continues to increase as this layer becomes a buoyant plume, accelerating because of its freshness and thus entraining more heat [Jenkins and Bombosch, 1995]. Melting and entrainment subsequently balance, and melting may decrease (even switching to freezing) because the freezing point increases, entrained water may be cooler (more modified from source water), and topography flattens (reducing plume speed and entrainment).

[71] Since the melt rate decreases toward the grounding line inshore of the tidal front, the mixed region insulates the grounding line from the source waters comprising the lower layers of the stratified ocean offshore. This study shows that this insulator is generally small and will be reduced or nonexistent in cavities that slope steeply toward the grounding line or are forced by warm waters or weak tides. Melting can occur closer to grounding lines in these cases, potentially increasing the vulnerability of the grounding line ice flux [Schoof, 2007]. It is interesting to note that, as far as observed, the thinning ice shelves fringing the Amundsen Sea generally have these characteristics.

## 5. Conclusions

[72] As the water column shallows toward ice shelf grounding lines, tidal mixing becomes more important until, beyond a tidal front, the water column is completely vertically homogenized. A highly simplified one-dimensional model of this mixed zone has been used to demonstrate some features of this theory. The study's motivations are to examine the length, properties, and sensitivities of these mixed zones and determine the melt rate variation near grounding lines.

[73] The main finding of this study is that tidally mixed zones near grounding lines are small in the vast majority of realistic scenarios; they only become significant under near-freezing conditions where the ocean cavity slope is shallow and tidal stirring is vigorous. Even these regions are predicted to be smaller than previously proposed. Near most grounding lines the customary view of a stratified ocean is adequate, with melting sustained by entrainment of heat into an upper mixed layer.

[74] The model predicts that within mixed zones the melt rate decreases as the grounding line is approached, so where present these regions act to insulate grounding lines from warmer waters offshore. Unlike the stratified ocean, the average melt rate in the small mixed zones increases linearly in response to ocean warming.

[75] The model includes many assumptions and is motivated toward these broad conclusions rather than detailed local questions. A fuller modeling effort would require attention to temporal variability, multidimensional tidal flow and residuals, complex cavity geometries, and subglacial

meltwater. Relaxing the assumptions of the present study could begin by addressing temporal variation in the location of tidal fronts.

[76] **Acknowledgments.** The author gratefully acknowledges useful comments from the reviewers and many colleagues and is particularly indebted to Keith Makinson for many enlightening discussions.

## References

- Albert, D. G., and C. R. Bentley (1990), Seismic studies on the grid eastern half of the Ross Ice Shelf: RIGGS III and RIGGS IV, in *The Ross Ice Shelf: Glaciology and Geophysics, Antarct. Res. Ser.*, vol. 42, edited by C. R. Bentley and D. E. Hayes, pp. 87–108, AGU, Washington D. C.
- Assmann, K., H. H. Hellmer, and A. Beckmann (2003), Seasonal variation in circulation and water mass distribution on the Ross Sea continental shelf, *Antarct. Sci.*, *15*, 3–11.
- Corr, H. F. J., C. S. M. Doake, A. Jenkins, and D. G. Vaughan (2001), Investigations of an 'ice plain' in the mouth of Pine Island Glacier, Antarctica, *J. Glaciol.*, *47*, 51–57.
- Craven, M., I. Allison, R. Brand, A. Elcheikh, J. Hunter, M. Hemer, and S. Donoghue (2004), Initial borehole results from the Amery Ice Shelf hot-water drilling project, *J. Glaciol.*, *39*, 531–539.
- Dinniman, M. S., J. M. Klinck, and W. O. Smith (2007), The influence of sea ice cover and icebergs on circulation and water mass formation in a numerical circulation model of the Ross Sea, Antarctica, *J. Geophys. Res.*, *112*, C11013, doi:10.1029/2006JC004036.
- Fearnhead, P. G. (1975), On the formation of fronts by tidal mixing around the British Isles, *Deep Sea Res.*, *22*, 311–321.
- Fischer, H. B., E. J. List, R. C. Y. Koh, J. Imberger, and N. H. Brooks (1979), *Mixing in Inland and Coastal Waters*, Academic, New York.
- Foster, T. D. (1983), The temperature and salinity finestructure of the ocean under the Ross Ice Shelf, *J. Geophys. Res.*, *88*, 2556–2564.
- Fricker, H. A., T. Scambos, R. Bindshadler, and L. Padman (2007), An active subglacial water system in West Antarctica mapped from space, *Science*, *315*, 1544–1548.
- Gade, H. G. (1979), Melting of ice in sea water; a primitive model with application to the Antarctic ice shelf and icebergs, *J. Phys. Oceanogr.*, *9*, 189–198.
- Gerdes, R., J. Determann, and K. Grosfeld (1999), Ocean circulation beneath Filchner-Ronne Ice Shelf from three-dimensional model results, *J. Geophys. Res.*, *104*, 15,827–15,842.
- Geyer, W. R., and R. P. Signell (1992), A reassessment of the role of tidal dispersion in estuaries and bays, *Estuaries*, *15*, 97–108.
- Gray, L., I. Joughin, S. Tulaczyk, V. Blue Spikes, R. Bindshadler, and K. Jezek (2005), Evidence for subglacial water transport in the West Antarctic Ice Sheet through three-dimensional satellite radar interferometry, *Geophys. Res. Lett.*, *32*, L03501, doi:10.1029/2004GL021387.
- Greischar, L. L., and C. R. Bentley (1980), Isostatic equilibrium grounding line between the West Antarctic inland ice sheet and the Ross Ice Shelf, *Nature*, *283*, 651–654.
- Greisman, P. (1979), On upwelling driven by the melt of ice shelves and tidewater glaciers, *Deep Sea Res., Part A*, *26*, 1051–1065.
- Hale, N. P. (2006), A sixth-order extension to the MATLAB bvp4c software of J. Kierzenka and L. Shampine, Master's thesis, Imperial Coll., London.
- Hearn, C. J. (1985), On the value of the mixing efficiency in the Simpson-Hunter  $hlu^3$  criterion, *Dtsch. Hydrogr. Z.*, *38*, 133–145.
- Heinart, M., and B. Riedel (2007), Parametric modelling of the geometrical ice-ocean interaction in the Ekstroemisen grounding zone based on short time-series, *Geophys. J. Int.*, *169*, 407–420.
- Hellmer, H. H., S. S. Jacobs, and A. Jenkins (1998), Oceanic erosion of a floating Antarctic glacier in the Amundsen Sea, in *Ocean, Ice, and Atmosphere: Interactions at the Antarctic Continental Margin, Antarct. Res. Ser.*, vol. 75, edited by S. S. Jacobs and R. F. Weiss, pp. 83–99, AGU, Washington D. C.
- Hemer, M. A., J. R. Hunter, and R. Coleman (2006), Barotropic tides beneath the Amery Ice Shelf, *J. Geophys. Res.*, *111*, C11008, doi:10.1029/2006JC003622.
- Holland, D. M., and A. Jenkins (1999), Modeling thermodynamic ice-ocean interactions at the base of an ice shelf, *J. Phys. Oceanogr.*, *29*, 1787–1800.
- Holland, D. M., S. S. Jacobs, and A. Jenkins (2003), Modelling the ocean circulation beneath the Ross Ice Shelf, *Antarct. Sci.*, *15*, 13–23, doi:10.1017/S0954102003001019.
- Holland, P. R., and D. L. Feltham (2006), The effects of rotation and ice shelf topography on frazil-laden Ice Shelf Water plumes, *J. Phys. Oceanogr.*, *36*, 2312–2327.
- Holland, P. R., A. Jenkins, and D. M. Holland (2008), The response of ice shelf basal melting to variations in ocean temperature, *J. Clim.*, *21*, 2558–2572.

- Holley, E. R., D. R. F. Harleman, and H. B. Fischer (1970), Dispersion in homogeneous estuary flow, *J. Hydraul. Div. Am. Soc. Civ. Eng.*, *96*, 1691–1709.
- Intergovernmental Panel on Climate Change (2007), *Climate Change 2007: The Physical Science Basis—Contribution of Working Group I to the Fourth Assessment Report of the Intergovernmental Panel on Climate Change*, 996 pp., Cambridge Univ. Press, Cambridge, U. K.
- Jacobs, S. S., A. R. Gordon, and J. L. Ardai (1979), Circulation and melting beneath the Ross Ice Shelf, *Science*, *203*, 439–443.
- Jacobs, S. S., H. H. Hellmer, C. S. M. Doake, A. Jenkins, and R. M. Frolich (1992), Melting of ice shelves and the mass balance of Antarctica, *J. Glaciol.*, *130*, 375–387.
- Jacobs, S. S., H. H. Hellmer, and A. Jenkins (1996), Antarctic Ice Sheet melting in the southeast Pacific, *Geophys. Res. Lett.*, *23*, 957–960.
- Jenkins, A. (1999), The impact of melting ice on ocean waters, *J. Phys. Oceanogr.*, *29*, 2370–2381.
- Jenkins, A., and A. Bombosch (1995), Modeling the effects of frazil ice crystals on the dynamics and thermodynamics of Ice Shelf Water plumes, *J. Geophys. Res.*, *100*, 6967–6981.
- Jenkins, A., and C. S. M. Doake (1991), Ice-ocean interaction on Ronne Ice Shelf, Antarctica, *J. Geophys. Res.*, *96*, 791–813.
- Jenkins, A., and D. M. Holland (2002), A model study of ocean circulation beneath Filchner-Ronne Ice Shelf, Antarctica: Implications for bottom water formation, *Geophys. Res. Lett.*, *29*(8), 1193, doi:10.1029/2001GL014589.
- Johnson, M. R., and A. M. Smith (1997), Seabed topography under the southern and western Ronne Ice Shelf, derived from seismic surveys, *Antarct. Sci.*, *9*, 201–208.
- Joughin, I., and L. Padman (2003), Melting and freezing beneath Filchner-Ronne Ice Shelf, Antarctica, *Geophys. Res. Lett.*, *30*(9), 1477, doi:10.1029/2003GL016941.
- Joughin, I., E. Rignot, C. E. Rosanova, B. K. Luccitta, and J. Bohlander (2003), Timing of recent accelerations of Pine Island Glacier, Antarctica, *Geophys. Res. Lett.*, *30*(13), 1706, doi:10.1029/2003GL017609.
- Kierzenka, J., and L. F. Shampine (2001), A BVP solver based on residual control and the Matlab PSE, *ACM Trans. Math. Softw.*, *27*, 299–316.
- Loynes, J., J. R. Potter, and J. G. Paren (1984), Current, temperature, and salinity beneath George VI Ice Shelf, Antarctica, *Deep Sea Res.*, *31*, 1037–1055.
- MacAyeal, D. R. (1984), Thermohaline circulation below the Ross Ice Shelf: A consequence of tidally induced vertical mixing and basal melting, *J. Geophys. Res.*, *89*, 597–606.
- Makinson, K. (2002a), Modelling tidal current profiles and vertical mixing beneath Filchner-Ronne Ice Shelf, Antarctica, *J. Phys. Oceanogr.*, *32*, 202–215.
- Makinson, K. (2002b), Tidal currents and vertical mixing processes beneath Filchner-Ronne Ice Shelf, Ph.D. thesis, Open Univ., Milton Keynes, U. K.
- Makinson, K., and K. W. Nicholls (1999), Modelling tidal currents beneath Filchner-Ronne Ice Shelf and on the adjacent continental shelf: Their effect on mixing and transport, *J. Geophys. Res.*, *104*, 13,449–13,465.
- Makinson, K., M. Schröder, and S. Østerhus (2006), Effect of critical latitude and seasonal stratification on tidal current profiles along Ronne Ice Front, Antarctica, *J. Geophys. Res.*, *111*, C03022, doi:10.1029/2005JC003062.
- Maslanyj, M. P. (1987), Seismic bedrock depth measurements and the origin of George VI Sound, Antarctic Peninsula, *Br. Antarct. Surv. Bull.*, *75*, 51–65.
- Nicholls, K. W. (1996), Temperature variability beneath Ronne Ice Shelf, Antarctica, from thermistor cables, *J. Geophys. Res.*, *101*, 1199–1210.
- Nicholls, K. W., K. Makinson, and A. V. Robinson (1991), Ocean circulation beneath the Ronne Ice Shelf, *Nature*, *354*, 221–223.
- Nicholls, K. W., K. Makinson, and M. R. Johnson (1997), New oceanographic data from beneath Ronne Ice Shelf, Antarctica, *Geophys. Res. Lett.*, *24*, 167–170.
- Nicholls, K. W., S. Østerhus, K. Makinson, and M. R. Johnson (2001), Oceanographic conditions south of Berkner Island, beneath Filchner-Ronne Ice Shelf, Antarctica, *J. Geophys. Res.*, *106*, 11,481–11,492.
- Nicholls, K. W., K. Makinson, and S. Østerhus (2004), Circulation and water masses beneath the northern Ronne Ice Shelf, Antarctica, *J. Geophys. Res.*, *109*, C12017, doi:10.1029/2004JC002302.
- Noh, Y., and H. J. S. Fernando (1995), Onset of stratification in a mixed layer subjected to a stabilizing buoyancy flux, *J. Fluid Mech.*, *304*, 27–46.
- Nøst, O. A. (2004), Measurements of ice thickness and seabed topography under the Fimbul Ice Shelf, Dronning Maud Land, Antarctica, *J. Geophys. Res.*, *109*, C10010, doi:10.1029/2004JC002277.
- O'Donnell, J. (1993), Surface fronts in estuaries: A review, *Estuaries*, *16*, 12–39.
- Okubo, A. (1967), The effect of shear in an oscillatory current on horizontal diffusion from an instantaneous source, *Int. J. Oceanol. Limnol.*, *1*, 194–204.
- Orsi, A. H., G. C. Johnson, and J. L. Bullister (1999), Circulation, mixing, and production of Antarctic Bottom Water, *Prog. Oceanogr.*, *43*, 55–109.
- Ou, H.-W., C.-M. Dong, and D. Chen (2003), Tidal diffusivity: A mechanism for frontogenesis, *J. Phys. Oceanogr.*, *33*, 840–847.
- Padman, L., H. A. Fricker, R. Coleman, S. Howard, and L. Erofeeva (2002), A new tide model for the Antarctic ice shelves and seas, *Ann. Glaciol.*, *34*, 247–254.
- Padman, L., S. Erofeeva, and I. Joughin (2003), Tides of the Ross Sea and Ross Ice Shelf cavity, *Antarct. Sci.*, *15*, 31–40, doi:10.1017/S0954102003001032.
- Payne, A. J., P. R. Holland, A. P. Shepherd, I. C. Rutt, A. Jenkins, and I. Joughin (2007), Numerical modelling of ocean-ice interactions under Pine Island Bay's ice shelf, *J. Geophys. Res.*, *112*, C10019, doi:10.1029/2006JC003733.
- Potter, J. R., and J. G. Paren (1985), Interaction between ice shelf and ocean in George VI Sound, Antarctica, in *Oceanology of the Antarctic Continental Shelf*, *Antarct. Res. Ser.*, vol. 43, edited by S. S. Jacobs, pp. 35–58, AGU, Washington, D. C.
- Potter, J. R., J. G. Paren, and M. Pedley (1985), Tidal behaviour under an Antarctic ice shelf, *Br. Antarct. Surv. Bull.*, *68*, 1–18.
- Rignot, E. J. (1998), Fast recession of a West Antarctic glacier, *Science*, *281*, 549–551.
- Rignot, E., and S. S. Jacobs (2002), Rapid bottom melting widespread near Antarctic Ice Sheet grounding lines, *Science*, *296*, 2020–2023.
- Schmeltz, M., E. Rignot, and D. R. MacAyeal (2001), Ephemeral grounding as a signal of ice-shelf change, *J. Glaciol.*, *47*, 71–77.
- Schoof, C. (2007), Ice sheet grounding line dynamics: Steady states, stability and hysteresis, *J. Geophys. Res.*, *112*, F03S28, doi:10.1029/2006JF000664.
- Shepherd, A. P., D. J. Wingham, and E. Rignot (2004), Warm ocean is eroding West Antarctic Ice Sheet, *Geophys. Res. Lett.*, *31*, L23402, doi:10.1029/2004GL021106.
- Simpson, J. H., and D. Bowers (1981), Models of stratification and frontal movement in shelf seas, *Deep Sea Res., Part A*, *28*, 727–738.
- Simpson, J. H., and J. R. Hunter (1974), Fronts in the Irish Sea, *Nature*, *250*, 404–406.
- Simpson, J. H., D. G. Hughes, and N. C. G. Morris (1985), The relation of seasonal stratification to tidal mixing on the continental shelf, in *A Voyage of Discovery*, edited by M. Angel, *Deep Sea Res.*, *24*, 327–340.
- Smith, A. M., and C. S. M. Doake (1994), Sea-bed depths at the mouth of Rutford Ice Stream, Antarctica, *Ann. Glaciol.*, *20*, 353–356.
- Soulsby, R. L. (1983), The bottom boundary layer of shelf seas, in *Physical Oceanography of Coastal and Shelf Seas*, edited by B. Johns, pp. 189–266, Elsevier, Amsterdam.
- Taylor, G. I. (1954), The dispersion of matter in turbulent flow through a pipe, *Proc. R. Soc. London, Ser. A*, *223*, 446–468.
- Weertman, J. (1974), Stability of the junction of an ice sheet and an ice shelf, *J. Glaciol.*, *13*, 3–13.
- Wingham, D. J., A. Shepherd, A. Muir, and G. J. Marshall (2006), Mass balance of the Antarctic Ice Sheet, *Philos. Trans. R. Soc. A*, *364*, 1627–1635, doi:10.1098/rsta.2006.1792.

P. R. Holland, British Antarctic Survey, High Cross, Madingley Road, Cambridge CB3 0ET, UK. (p.holland@bas.ac.uk)